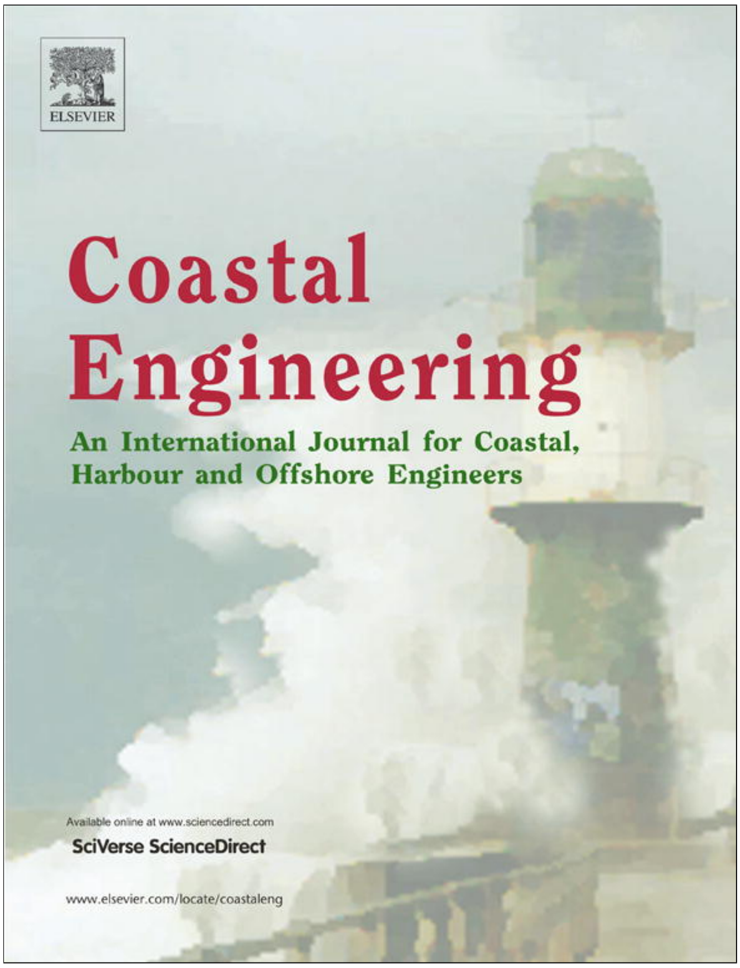
ELSEVIER
Coastal Engineering
An International Journal for Coastal, Harbour and Offshore Engineers
Available online at www.sciencedirect.com
SciVerse ScienceDirect
www.elsevier.com/locate/coastaleng

Coastal Engineering 79 (2013) 9–21

Contents lists available at SciVerse ScienceDirect

Coastal Engineering

journal homepage: www.elsevier.com/locate/coastaleng

Tsunami inundation modeling in constructed environments: A physical and numerical comparison of free-surface elevation, velocity, and momentum flux

Hyoungsu Park [a,*], Daniel T. Cox [a], Patrick J. Lynett [b], Dane M. Wiebe [a], Sungwon Shin [c]

[a] School of Civil and Construction Engineering, Oregon State University, Corvallis, OR 97331-2302, USA
[b] Dept. of Civil and Environmental Engineering, University of Southern California, Los Angeles, CA 90089-2531, USA
[c] Department of Energy Plant, College of Engineering, Kwandong University, 522 Naegok-dong, Gangneung, Gangwon-do 210-701, South Korea

ARTICLE INFO

Article history:
Received 29 October 2012
Received in revised form 3 April 2013
Accepted 8 April 2013
Available online xxxx

Keywords:
Tsunami
Inundation
Macro-roughness
Benchmark
COULWAVE
Friction factor

ABSTRACT

A laboratory benchmark test for tsunami inundation through an urban waterfront including free surface elevation, velocity, and specific momentum flux is presented and compared with a numerical model (COULWAVE). The physical model was a 1:50 scale idealization of the town Seaside, Oregon, designed to observe the complex tsunami flow around the macro-roughness such as buildings idealized as impermeable, rectangular blocks. Free surface elevation and velocity time series were measured and analyzed at 31 points along 4 transects. Optical measurements of the leading bore front were used in conjunction with the in-situ velocity and free surface measurements to estimate the time-dependent specific momentum flux at each location. The maximum free surface elevation and specific momentum flux sharply decreased from the shoreline to the landward measurement locations, while the cross-shore velocity slowly decreased linearly. The experimental results show that the maximum specific momentum flux is overestimated by 60 to 260%, if it is calculated using the each maximum values of the free surface elevation and cross-shore velocity. Comparisons show that the numerical model is in good agreement with the physical model at most locations when tuned to a friction factor of 0.005. When the friction factor decreased by a factor of 10 (from 0.01 to 0.001), the average maximum free surface elevation increased 15%, and the average cross-shore velocity and specific momentum flux increased 95 and 208%, respectively. This highlights the importance of comparing velocity in the validation and verification process of numerical models of tsunami inundation.

1. Introduction

Tsunamis are unpredictable natural events which are most commonly associated with large magnitude earthquakes along coastal plate boundaries. For near field events, the first waves often arrive in the tens of minutes, leaving little time for preparation or evacuation, and can inundate several kilometers inland. Tsunamis, such as the 2004 Indian Ocean event, delivered widespread damage to coastal communities both near and far from the epicenter, and caused casualties in the hundreds of thousands, which is devastating both locally and regionally (Imamura et al., 2006). The most recent tsunami occurred on March 11th, 2011 in the north-western Pacific Ocean 72 km east of the Oshika Peninsula of Tōhoku, Japan. This event resulted in 15,844 fatalities 3394 missing peoples and damaged 128,530 houses, 230,332 buildings and 78 bridges (Mori et al., 2011).

To minimize casualties and damage from future events, a deeper understanding of tsunamis is required, particularly for the complex flows associated with the tsunami inundation and the return flow over complex bathymetry and around structures. Due to the increasing computational power and maturation of numerical schemes, the numerical modeling of tsunami inundation is becoming increasingly important for tsunami mitigation (e.g., Lynett, 2007). However, some simplifications of the numerical schemes are required, particularly with respect to the problem of turbulence closure, and to extend the model over a sufficiently large domain (e.g., several km to encompass a coastal community).

To model the tsunamis hazard for coastal communities accurately, the constructed environment must be incorporated into the numerical model as it strongly influences the hydrodynamics. The 2004 Indian Ocean Tsunami field survey highlighted the importance of coastal structures in mitigating tsunami damage (Dalrymple and Kribel, 2005; Tomita et al., 2006). After the 2011 Great East Japan Tsunami, the field survey also highlighted that tsunami damage is strongly dependent on location and environment (Yeh et al., in press). Yeh (2006) showed that the hydrodynamic force of the tsunami on structures in the inundation zone is proportional to the momentum flux, which is the inundation depth multiplied by the squared velocity and it can be related to the probability of damage (e.g., FEMA, 2008; Koshimura et al., 2009a, 2009b).

* Corresponding author. Tel.: +1 541 602 8618; fax: +1 541 737 3052.
E-mail addresses: Hyoungsu.park@gmail.com (H. Park), dan.cox@oregonstate.edu (D.T. Cox), plynett@usc.edu (P.J. Lynett), wiebed@onid.orst.edu (D.M. Wiebe), sungwshin@gmail.com (S. Shin).

0378-3839/$ – see front matter
http://dx.doi.org/10.1016/j.coastaleng.2013.04.002

It is also necessary to benchmark these models' performance in terms of predicting the free surface and velocity as well as their sensitivity to tuning parameters. Several benchmark tests are prevailing as standard verification methods for the numerical modeling of tsunamis (Liu et al., 2008; Synolakis et al., 2007; Yeh et al., 1996) such as exact solutions and physical model data of solitary waves on simple sloped beaches (Synolakis, 1987) and on compound sloped beaches (Kânoğlu and Synolakis, 1998), large scale conical island physical model (Briggs et al., 1995), and runup on a complex three-dimensional coast (Hokkaido Tsunami Survey Group, 1993). In addition, landslide tsunamis generated by submarine mass failure received much attention after the 1998 Papua New Guinea tsunami, and a three dimensional landslide experiment (Synolakis, 2003) was performed as a benchmark test. Even though most casualties and damage from tsunamis are related to the complex inundation flow, which includes wave breaking near the shoreline and interaction with coastal structures, the most advanced numerical models and benchmark tests only provide the maximum run-up heights or a time series of free surface elevation. Complex flows are difficult both to estimate due to the required computing power and validate due to the absence of proper benchmark tests. As a result, most numerical models focused on the estimation of tsunami propagation, and calculation of arrival times and maximum runup heights.

Several studies related to macro-roughness and tsunami velocity variation have been performed. Cox et al. (2008) performed physical model tests of Seaside, Oregon, which showed that the macro-roughness reduced the tsunami inundation velocity by 40% (Rueben et al., 2010). The reduction in runup elevations and maximum overland velocities due to obstructions have been studied numerically (Lynett, 2007) and Tomita and Honda (2007) highlighted that the resulting inundation area and depth from the numerical model with macro-roughness was in good agreement with the actual inundation observed in Galle city, Sri Lanka from the 2004 Indian Ocean tsunami. Other studies on the influence of macro-roughness element arrays compared the free surface elevation of numerical and physical model results (Goseberg and Schlurmann, 2010), and the effect of bed slope and bottom friction on maximum tsunami runup height and velocity using numerical models (Apotsos et al., 2011). More recently, the importance of artificial and natural structures on tsunami mitigation was studied through a numerical and field study (Nandasena et al., 2012).

In this project, we present a model study of tsunami flow over and around macro-roughness in the idealized physical model of Seaside, Oregon, and provide a new data set of free surface elevation, velocity, and momentum to be used as a benchmark test. This data set was used to validate the numerical model results from COULWAVE (Lynett et al., 2002). This paper is outlined as follows. Section 2 presents the large-scale physical model basin, measurement devices and their locations, describes the model data analysis, and shows the results of the experiment. Section 3 presents the numerical model setup. Section 4 presents a comparison between the physical and numerical model. Section 5 concludes the paper with summary findings and ideas for future work.

2. Model design setup

The physical model was an idealized representation of Seaside, Oregon, located in the Pacific Northwest, United States constructed at 1:50 undistorted scale. There are several reasons why this site was chosen for study. One, the Cascadia Subduction Zone (CSZ) has a high potential hazard for the tsunami event in near future. Over the past 10,000 years the CSZ has shown three typical rupture scenarios: a rupture of 200–450 km of the southern margin with 18–20 events on the order of 8.2 Mw, a rupture of 650 km starting at the southern margin with 3–4 events on the order of 8.5 Mw, and a full length rupture with 19–20 events on the order of 8.9 Mw (Goldfinger et al., 2012). The average recurrence interval between CSZ events is 240 years, and the next event is estimated to have a 7–12% probability of occurrence in the next 50 years (Goldfinger et al., 2012). Two, the CSZ has the simple bathymetry of shore parallel contours and a large onshore spit. And three, the high concentration of residential and commercial buildings concentrated near the water front and located well within the expected tsunami inundation zone. Fig. 1 shows the expected extent of inundation from the CSZ event tsunami (solid line) (DOGAMI, 2001), the dimensions of the physical model basin (dash–dot line), and the dimensions of the physical model with macro-roughness (dashed line). The inset map within Fig. 1 shows the location of Seaside, Oregon, on a

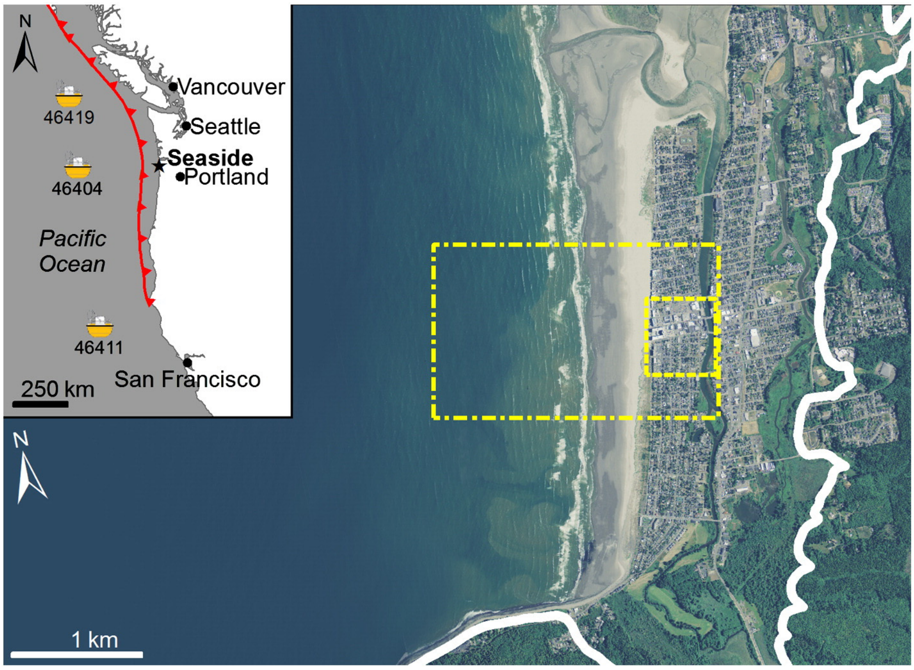

Fig. 1. Seaside, Oregon, Main map (source from Google) shows the 1:50 physical model region (dash–dot), macro-roughness region (dash), and tsunami inundation line (solid). Inset map shows regional location of Seaside, location of offshore DART buoys, and proximity to the Cascadia subduction zone (solid-triangle).

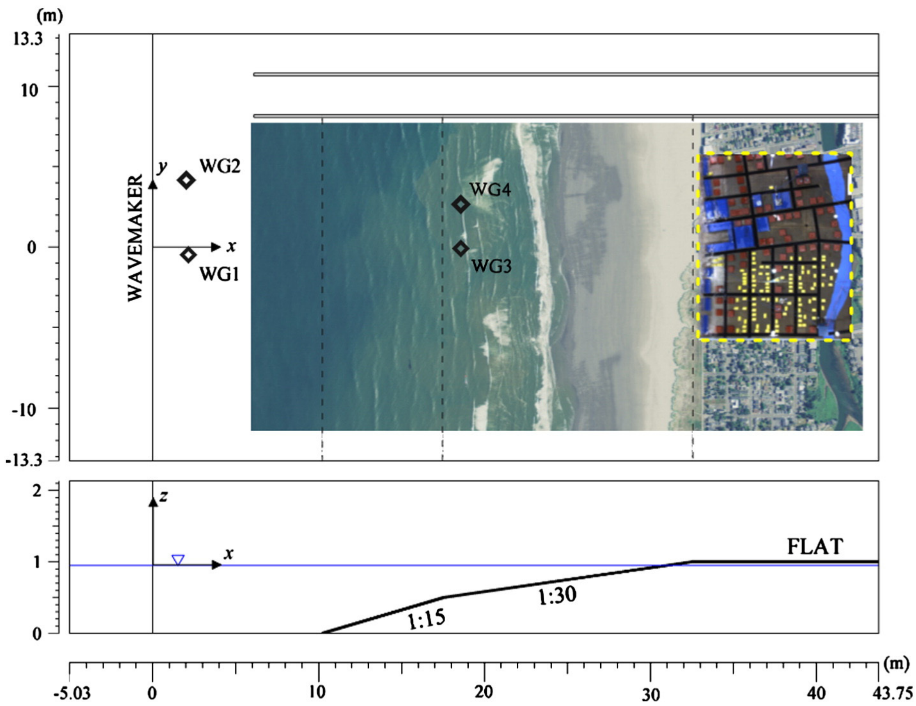

Fig. 2. Plan and elevation view of the physical model in the Tsunami Wave basin. Satellite imagery (Source from Google) and a laboratory photo provide the scale of the Seaside, OR, model.

region scale, the proximity to the CSZ, and the location of the Deep-ocean Assessment and Reporting of Tsunamis (DART) buoys (NOAA, 2012).

Plan and elevation views of the physical model in the Tsunami Wave Basin at O.H. Hinsdale Wave Research Laboratory, Oregon State University, are shown in Fig. 2. The background images are satellite imagery of Seaside and a photo of the top view of the physical model (Rueben et al., 2010). The origin of the x and y axes was centered on the wavemaker, with the x positive onshore and the y positive to the north. The rectangular basin was 48.8 m long, 26.5 m wide, and 2.1 m deep, and was equipped with a segmented, piston-type wavemaker with a maximum stroke of 2.1 m and maximum velocity of 2.0 m/s (Cox et al., 2008). The idealized bathymetry for Seaside was constructed of smooth concrete with a flat finish, and an estimated roughness height of 0.1–0.3 mm (Rueben et al., 2010). The profile consisted of a 10 m horizontal section near the wavemaker with a depth of 0.97 m, an 8 m section at a 1:15 slope, a 15 m section at a 1:30 slope, on which the SWL intersected, and another horizontal section 11 m in length which extended to the back wall. The idealized buildings which created the macro-roughness elements were fixed in place on the upper horizontal section to provide repeatability between tests. Four surface piercing wire resistance wave gages (WG1–WG4) were fixed in the basin at the following locations: WG1 (2.086 m, −0.515 m), WG2 (2.068 m, 4.065 m), WG3 (18.618 m, 0.000 m), and WG4 (18.618, 2.860 m).

A detailed plan view of the macro-roughness elements is shown in Fig. 3 in the same orientation as Figs. 1 and 2, with the Pacific Ocean to the left. In the model, the town is fronted by a 2 m (prototype scale) seawall. The blocks represent large hotels or commercial buildings, light commercial buildings, and residential houses, and the thick solid black lines between the blocks represent city streets. The buildings were positioned on the flat ground using aerial imagery and field survey data. The Necanicum River which flows through the center of Seaside ($x = 42$ m), was not included in the model, and is only referenced with blue paint. Other parameters not taken into account by the physical model include vegetation, debris, sediment, and other small-scale roughness effects. The white boxes labeled A to D and 1 through 9, represent measurement locations of free surface elevation and velocity. Measurement locations are divided into 4 lines; A to D. Line A is located on a city street parallel to the primary inundation flow direction and numbered sequential 1 to 9, as the measurement locations move inland. Lines B and C are on streets inclined approximately 10° to the flow direction, are flanked by hotels or commercial buildings, and numbered the same as line A. Line D is located mostly behind buildings and only had 4 measurement locations. In total there were 31 measurement locations.

Four pairs of co-located ultra-sonic surface wave gages (USWG, Senix Corporation TS-30S1-IV) and acoustic-Doppler velocimeter (ADV, Nortec Vectrino) sensors were used to measure the free surface and flow velocity in lines A, B, C, and D, simultaneously. Through the experiment, the sensors in lines A, B, and C moved in unison from positions 1 through 9 and have the same number of repetitions for lines A, B, and C at a given location as indicated in Table 1. The sensors in line D moved somewhat independently as listed in Table 1 with the aim of extracting turbulence statistics although this proved to be problematic due to the initial air entrainment. For the single tsunami wave condition, the total number of trials, N_T, was 136, of which the total number of acceptable trials, N_V, which were suitable for analysis was 99. The majority of trials ($N_T = 53$) were performed with all the sensors located at position 1 to collect statistics of turbulence due to the wave breaking. Because of time constraints, the number of trials performed at the remaining locations decreased; however, an adequate number of trials were still performed to provide reliable ensemble averages. Table 1 lists the coordinates of each measurement location and the total number of trials performed and available. Again, the origin of the coordinates is the center of the wavemaker (Fig. 2).

The design tsunami condition produced by the wavemaker used an error function to maximize the full 2.0 m stroke, and had a duration of 10.0 s. The wave height measured at WG1, over the horizontal section of the basin, was approximately 0.20 m. At prototype scale, this wave height is 10 m, which corresponds to the estimated tsunami wave height for the “500-yr” CSZ tsunami for this region (Tsunami Pilot Study Working Group, 2006).

2.1. Model results

This section presents the measured time dependent and cross-shore variability of maximum free surface displacement, velocity, and

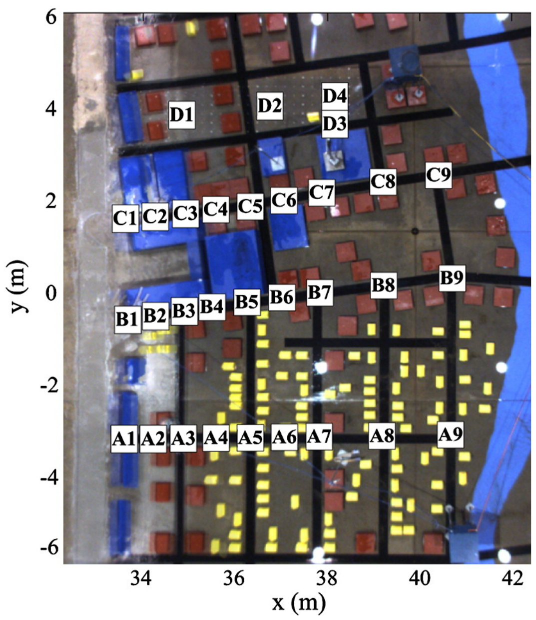

Fig. 3. Detailed plan view of macro-roughness elements of the physical model, annotated with measurement locations. (For interpretation of the references to color in this figure, the reader is referred to the web version of this article.)

momentum flux. Fig. 4a shows the wave-maker paddle displacement, S (solid line), as a function of time and the free surface elevation on the paddle (dashed line) for Trial 51. Fig. 4b shows the measured time series of free surface elevation at WG1 (solid line) and WG3 (dashed line) for Trial 51. WG 1 and 3 were located 2.0 m and 18.6 m from the wavemaker, and had peak elevations of 0.17 and 0.20 m, respectively. The shape of wave at WG3 was asymmetric and pitched forward as it passed the change in bathymetry. At $t = 35$ s, reflected waves were detected at WG3 due to wave interaction on the shoreline and front row of buildings. The variability between runs can be estimated by comparing the standard deviation of the signal to the full scale value. In Table 2, σ_i is the standard deviation at the maximum of the ensemble averaged value and i is the time corresponding to the maximum ensemble averaged value. $(X_i)_m$ is the full scale value at that time. For consistency, the statistics were computed using only the first 20 runs for each of the values listed in Table 2 although some quantities has a much larger number of realizations. Comparisons are made of the ratio of the standard deviation of the signal at the time of the maximum value to maximum ensemble averaged value, $\sigma_i/(X_i)_m$ expressed as a percent. The variability is extremely low for the wavemaker displacement (0.14%), and low for the free surface elevation measured before breaking in the middle of the basin (less than 1.2%). After breaking, the variability increases to approximately 5% of the full scale value. The largest variation at D4 (8.2%) occurs behind the second row of buildings in the area where large eddies were observed. Fig. 4c and d show the time series of free surface elevation and cross-shore velocity for Trial 51 at A1 (solid line) and C1 (dash line). The maximum free surface elevation, $(\eta)_m$, and maximum cross-shore velocity, $(u)_m$, were 0.25 and 0.18 m and 1.45 and 1.85 m/s at A1 and C1, respectively. The USWG and ADV sensors were intended to measure the instantaneous velocity over land; however, the ADV sensor only detected velocities after $t = 26.4$ s, which was 1.3 s after the USWG sensor recorded the changes in the free surface elevation. The leading edge velocity was determined using optical measurements (Rueben et al., 2010) and an interpolation was used to replace the missing velocity data as explained in the next paragraph.

Fig. 5a shows the time series of ensemble averaged free surface elevation, $<\eta>$, ensemble averaged cross-shore velocity, $<u>$, and ensemble averaged momentum flux per unit mass per unit width, $<M>$, at A1. The momentum flux per unit mass per unit width, hereafter called the specific momentum flux for brevity, is generally calculated as Hu^2, where H is the total water depth, calculated by subtraction of vertical datum, h, from free surface elevation, η. Assuming Froude similitude would govern the scaling of the specific momentum flux (Hughes, 1993), the momentum flux per unit mass per unit width shown in Figs. 5 and 6 would be proportional to the length scale squared or would be multiplied by 2.5×10^3 to convert to prototype conditions. Fig. 5b shows the number of recorded data for free surface elevation, N_η, and cross-shore velocity, N_u, at each time step for location A1. The total number of available trials, N_V, at A1 was 48 (Table 1). For the USWG, there were some dropouts in the free surface measurements before the arrival of the bore ($t < 25.1$ s) and the number of available measurements was approximately $N_\eta = 40$. After arrival of the bore, the sensor accurately captured the free surface elevation and $N_\eta = N_V = 48$. For the ADV, due to air entrainment in the leading edge of the bore, no data were collected for $25.1 < t < 26.4$ s. After 26.4 s, the number of trials for which data were available increased as shown in Fig. 5b (open circles) with $N_u > 40$ at around $t = 28.5$ s, leading to a stable estimate of the velocity as can be seen in Fig. 5a. To obtain an estimate of the missing data, the leading wave velocities were analyzed by tracking the leading edge trajectory of each time step using two high resolution video cameras mounted on the ceiling of the wave basin (Rueben et al., 2010).

A second order polynomial curve (slender lines) was fit from the leading velocity (filled circle) to the ensemble averaged ADV data at

Table 1
Measurement locations and numbers of total and available trials, N_T and N_V, respectively.

Num.	Line A		Line B		Line C		A, B, & C		Num.	Line D			
	x (m)	y (m)	x (m)	y (m)	x (m)	y (m)	N_T	N_V		x (m)	y (m)	N_T	N_V
1	33.61	−3.19	33.72	−0.59	33.81	1.51	53	48	1	35.12	3.71	53	48[a]
2	34.10	−3.19	34.22	−0.53	34.55	1.60	11	10	2	36.68	3.89	33	26[b]
3	34.53	−3.18	34.68	−0.47	35.05	1.69	12	12					
4	35.04	−3.18	35.18	−0.41	35.56	1.77	12	4					
5	35.54	−3.19	35.75	−0.32	36.05	1.85	18	5	3	38.09	4.07	18	5[c]
6	36.35	−3.20	36.64	−0.23	37.05	1.99	7	6	4	38.14	3.59	28	20[d]
7	37.76	−3.20	37.77	−0.07	38.24	2.19	6	3					
8	39.22	−3.20	39.22	0.14	39.21	2.34	8	7					
9	40.67	−3.23	40.67	0.27	40.40	2.58	9	4					
Total							136	99				136	99

Ensemble averaged data at all 31 measurement locations are available by contacting the first author.
[a] Corresponds to lines A to C Num. 1.
[b] Corresponds to lines A to C Num. 2, 3 and 4.
[c] Corresponds to lines A to C Num. 5.
[d] Corresponds to lines A to C Num. 6, 7, 8 and 9.

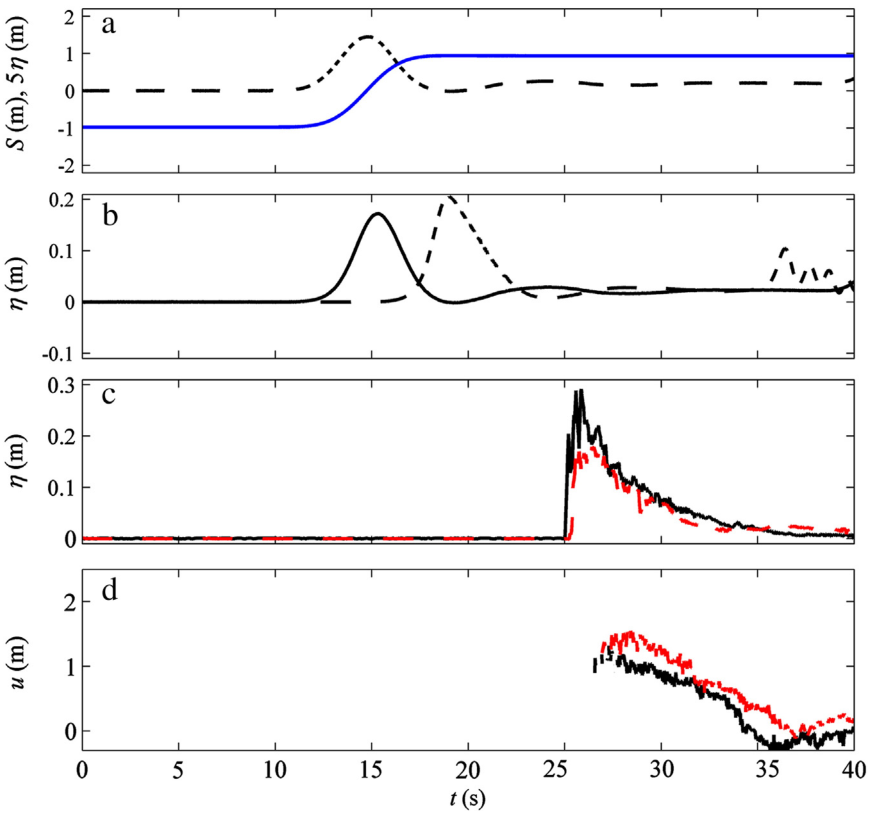

Fig. 4. Time series plots for Trial 51. (a) Wave-maker paddle displacement, S, (solid line) and free surface elevation on paddle multiplied by a factor of 5, 5η (dashed line. (b) η, at WG1 (solid line) and at WG3 (dashed line).(c) η at A1 (solid line) and at C1 (dashed line). (d) u at A1 (solid line, down) and at C1 (dashed line, upper).

$t = 28.5$ s. The velocity was assumed to increase linearly from zero (recorded by the USWG) to the leading edge velocity. The ensemble averaged specific momentum flux <M> was estimated from the ensemble estimates of the total water depth and the measured and interpolated velocity,

$$\langle M \rangle = \langle H \rangle \bullet \langle u \rangle^2.$$

The same procedure was performed at each measurement location, and the results at A8 are shown in Fig. 6. For A8, the ADV was able to capture more of the leading wave velocity because there was less air entrainment at A8. However, there was still some missing velocity data, and the same curve fitting procedure was used. The work of Rueben et al. (2010) successfully estimated the leading velocity for the same experimental setup using two overhead cameras with overlapping fields of view to capture the inundation along the length of the basin from $25 < x < 43$ m and from $-7 < y < 7$ m across the basin where the x and y coordinates are defined in Fig. 2 and includes the area shown in Fig. 3. The two cameras were synchronized, and the images were rectified to the known elevation of the model at 1 m above the basin floor. The arrival time of the bore at locations in the image corresponding to the sensor positions were compared to the arrival time measured by the sensors themselves to assure the accuracy of the optical measurement in predicting the spatial and temporal variation of leading edge. The velocity was constructed by taking the difference of successive frames as explained in Rueben et al. (2010) and was used here to provide the velocity at the leading edge which was not captured by the in-situ instruments.

As the wave propagated around the macro-roughness, properties such as wave shape and the location of maximum free surface elevation, cross-shore velocity, and specific momentum flux, changed (Figs. 5 and 6). The maximum free surface elevation and cross-shore velocity decreased from A1 to A8 from 0.25 to 0.06 m and 2.3 to 1.6 m/s, respectively. As the wave inundated the land, the location of maximum free surface elevation occurred later in time, but the location of maximum velocity remained at the front part of the wave. The maximum specific momentum flux decreased from A1 to A8 from 0.82 to 0.05 m^2/s^3, and the locations did not coincide with either the maximum velocity or free surface elevation. Similar to the maximum free surface elevation, the location of the maximum specific momentum flux also transitioned from the front to the rear of wave as it propagated over the land.

Note that the specific momentum flux, M, are calculated by multiplying each time series of H by u^2, and the maximum specific momentum flux, $(M)_m$, taken as the maximum value over the time series. However, if $(M)_m$ were to be calculated by multiplying the maximum value of H and, u then $(M)_m$ would be overestimated by approximately 60% at A1 and 260% at A8. The importance of correctly estimating the maximum momentum flux as it relates to hydrodynamic force on infrastructure has been discussed by FEMA (2008).

Table 2
Standard deviation of the signal to the full scale value for the wavemaker (S), free surface prior to breaking (WG 1, 3) and after breaking (A1, D1, D4).

Variables	σ_i	$(X_i)_m$	$\sigma_i/(X_i)_m$
	[m]	[m]	[−]
S	0.0002	1.889	0.14
WG1	0.0017	0.170	0.99
WG3	0.0023	0.201	1.13
A1	0.0149	0.271	5.50
D1	0.0027	0.052	5.11
D4	0.0038	0.046	8.25

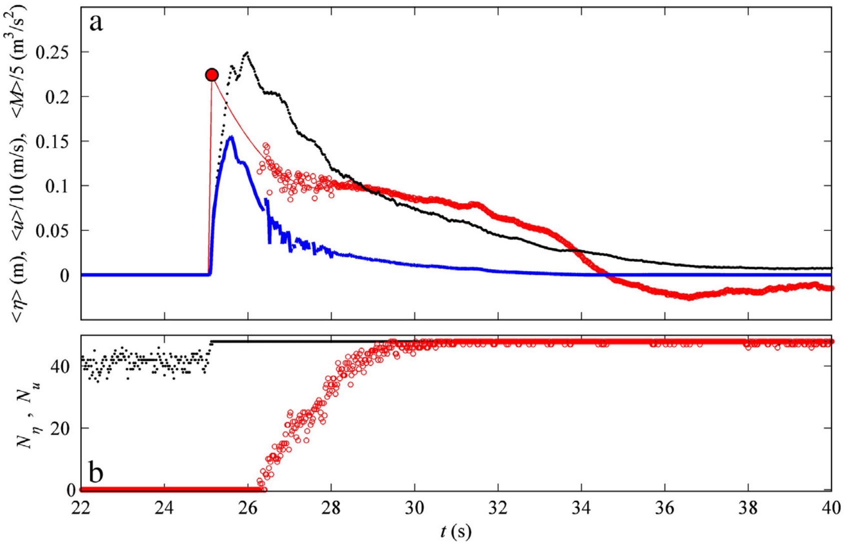

Fig. 5. Measured and calculated inundation flow data at A1. (a): Ensemble averaged free surface elevation, <η> (dot), ensemble averaged velocity, <u> (circle), ensemble averaged specific momentum flux, <M> (thick line), leading wave velocity from optical measurement, u_L (filled circle), fitted curve for <u> (slender line). (b): Number of recorded free surface elevation at each time step, N_η (dot) and number of recorded cross-shore velocity at each time step, N_u (circle). Number of data recorded at each time step from USWG (dot) and ADV (circle).

3. Numerical model

There is a wide range of numerical models that could be used to simulate the Seaside experiments. Depth-integrated models, such as those based on the nonlinear shallow water (e.g. Titov and Synolakis, 1995) or Boussinesq-type (e.g. Shi et al., 2012) equations are commonly used to simulate overland tsunami flow. Here, we use the model COULWAVE which solves a Boussinesq set of equations and approximately includes the effects of bottom-stress-driven turbulence with the associated vorticity (Kim et al., 2009) and small-scale turbulent mixing (Kim and Lynett, 2011). The governing equations will not be repeated here, but can be found with details in the above references. A high-order finite-volume numerical solution scheme is employed to solve the conservative-form equations, and the model has been validated for wave overtopping of structures and interaction with steep slopes (Lynett et al., 2010).

For the simulations presented in this paper, the wave basin is discretized with a constant and uniform grid of 5 cm and consisted of 872 by 432 points. The wave is generated along the offshore boundary by implementing a wavemaker-type condition (horizontally moving vertical wall) and is forced with the wavemaker trajectory measured during the experiment. The bathymetry and topography grid employs the lidar-surveyed data taken during the experiment, spatially averaged to fit the coarser numerical grid. It is important to note here that the individual structures and buildings in the town are approximated as steep-sided topography; while in reality the sides of these buildings are vertical they are not numerically modeled as such. Many of the buildings are overtopped by the wave, and it is

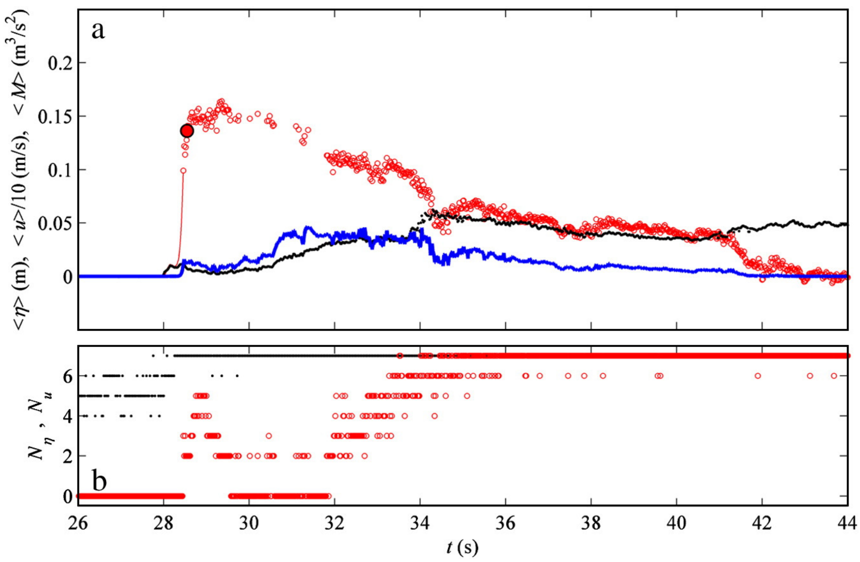

Fig. 6. Measured and calculated inundation flow data at A8. (a): Ensemble averaged free surface elevation, <η> (dot), ensemble averaged velocity, <u> (circle), ensemble averaged specific momentum flux, <M> (thick line), leading wave velocity from optical measurement, u_L (filled circle), and interpolated velocity (slender line). (b): Number of recorded free surface elevation at each time step, N_η (dot) and number of recorded cross-shore velocity at each time step, N_u (circle). Number of data recorded at each time step from USWG (dot) and ADV (circle).

very difficult to numerically implement a vertical wall boundary condition and simultaneously allow dynamic overtopping. Therefore, the maximum bottom slope found in the domain can be controlled by the grid resolution, and here any side slope that exceeds 2:1 (~63°) is smoothed until no longer this steep. Physical implications of this steep-slope approximation include an incorrect prediction of flow properties that are dependent on locally steep slopes, such as strong vertical acceleration, uprush, and overtopping. However, results have been checked for grid-length-dependent numerical convergence.

The breaking model used is that described in Lynett (2006), which is very similar to the scheme given in Kennedy et al. (2000). Bottom stress is calculated with the common quadratic friction law, i.e. $\frac{\partial u}{\partial t} + \cdots + \frac{f u|u|}{H} = 0$, where the dimensionless friction factor, f, is given as an input value, constant in both space and time throughout the simulation. The stochastic backscatter model presented in Kim and Lynett (2011) is not used in the simulations presented here. The full Boussinesq-type set of equations are solved at all points in the domain; there is no switch-off of high-order terms over initially dry grid points.

4. Comparison of results and discussions

The majority of previous benchmark tests for inundation models typically compare a time series of free surface elevation or maximum run-up height, but in this study, the time series and maximum values of free surface elevation, cross-shoreline velocity, and specific momentum flux are extracted from the numerical model and directly compared with the physical model results for model verification.

A time series comparison of $<\eta>$, $<u>$ and $<M>$ between the physical model (dotted line) and numerical model (COULWAVE) (solid line) at B1, B4, B6, and B9 (line B is parallel to the flow direction and flanked by hotels and commercial buildings) are shown in Figs. 7, 8, and 9, respectively. There are local disagreements in free surface elevation and specific momentum flux comparison, but general tendencies and magnitudes were well matched with physical model results. Specifically, COULWAVE underestimates the free surface elevation at B1 and B4, whereas at B9 it overestimates the value. However, for specific momentum flux, COULWAVE underestimates the value at B1, and overestimates at B6 and B9.

To calibrate COULWAVE for these comparisons, three different friction factors, $f = 0.001$, 0.005, and 0.01 were tested. A friction factor of $f = 0.005$ was found to produce results most similar to the physical model and was used for all subsequent analysis. The expected differences due to friction factors will be discussion in more detail in Section 4.1.

Reflection from the model boundaries was simulated by COULWAVE. The back end of the tank in the numerical model is at a different x location than in the physical model study, and the reflection off this back wall arrives at the measurement locations earlier. Therefore, reflection effects produced by COULWAVE resulted in some erroneous data when compared to the physical model which is shown in Figs. 7, 8, and 9 (dotted lines). For example, in Fig. 7d, the magnitude of free surface elevation from COULWAVE was nearly twice as large as the physical model values due to reflection. Reflection wave effects are also observed in cross-shore velocity and specific momentum flux in Figs. 8 and 9. Fig. 10 compares the maximum free surface elevation, cross-shore velocity and specific momentum flux between the numerical and physical model from B1 to B9. The x-axis represents the distance to each measurement location (B1 to B9) in the x-direction from the origin, B1. The maximum values of $<\eta>$, $<u>$ and $<M>$ were extracted at each location, and therefore, do not necessarily correspond to the same instant in time. Reflection effects present in the numerical model were excluded in the maximum value comparison. Within the first 1.5 m, there are minor disagreements in $<\eta>$ and $<M>$, however the numerical model values of $<M>$ show the same abrupt decrease and increase pattern between 0 and 1 m as the physical model. Overall the physical and numerical model show good agreement. In both models, it is observed that the maximum free surface elevation and specific momentum flux sharply decrease from the shoreline as the measurement location moves landward, while the cross-shore velocity slowly decreases linearly. Specifically, from B1 to B9, the maximum free surface elevation, $(\eta)_m$ decreases 72%, the maximum momentum flux, $(M)_m$ decreases 96% and the maximum cross-shore velocity, $(u)_m$ decreases 41% in the physical model.

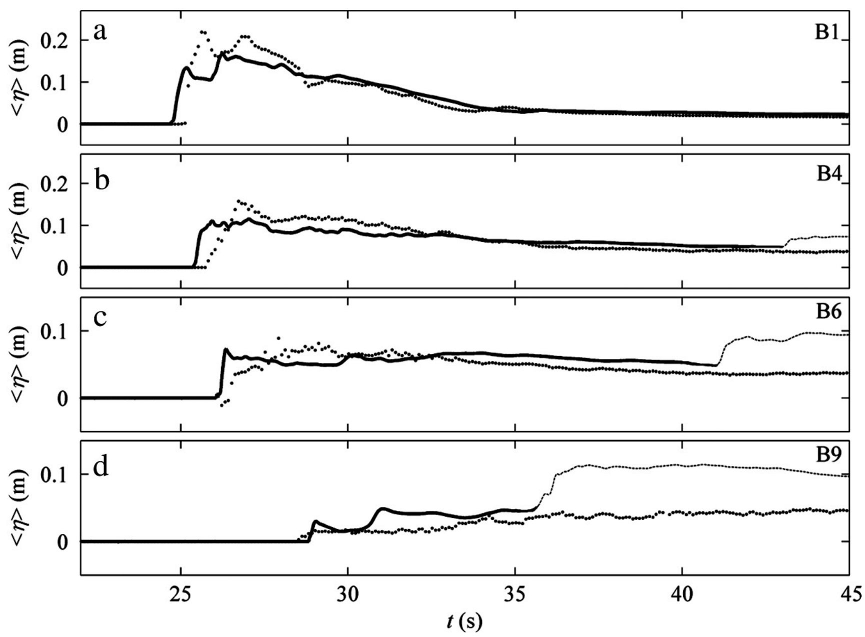

Fig. 7. Comparison of $<\eta>$ between physical model (dot) and numerical model (solid line) at B1, B4, B6 and B9. Where wave reflection is present in the numerical model, the solid line switches to a dashed line.

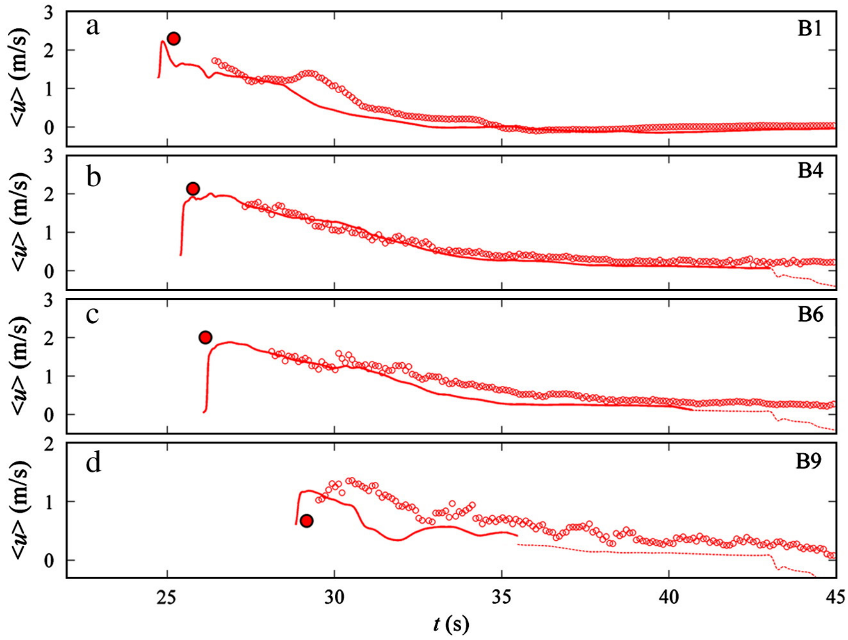

Fig. 8. Comparison of <u> between physical model (circle) and numerical model (solid line) at B1, B4, B6 and B9 with the leading velocity from optical measurement (filled circle). Where wave reflection is present in the numerical model, the solid line switches to a dashed line.

Fig. 11 shows the normalized root mean square errors of the numerical model compared to the physical model at each measurement location for η, u, and M, respectively. The normalized root mean square errors are evaluated as:

$$NRMSE(\phi)\frac{\sum_{i=1}^{r}\left(\hat{\phi}_i - \phi_i\right)^2}{\phi_{max} - \phi_{min}}$$

where $\hat{\phi}_i$ is the numerical model value, ϕ_i is the physical model value, ϕ_{max} and ϕ_{min} are the maximum and minimum from the physical model, r is the time step number which is less than 1% of the maximum free surface elevation or the time step number when reflection effects first appear, and the i is the time step for each value of η, u, and M. The normalized root mean square errors for the free surface elevation at lines A, B, and C are within 0.1, except at C1 where it increased to 0.2, and for line D where the numerical model results overestimated the values and are approximately 0.3 to 0.4 (Fig. 11a). Most of the normalized root mean square errors of cross-shore velocity for lines A and D were less than 0.4, and for lines B and C less than 0.2 (Fig. 11b). In the case of specific momentum flux, with the exception of line D which measured around 0.8, most values are less than 0.2.

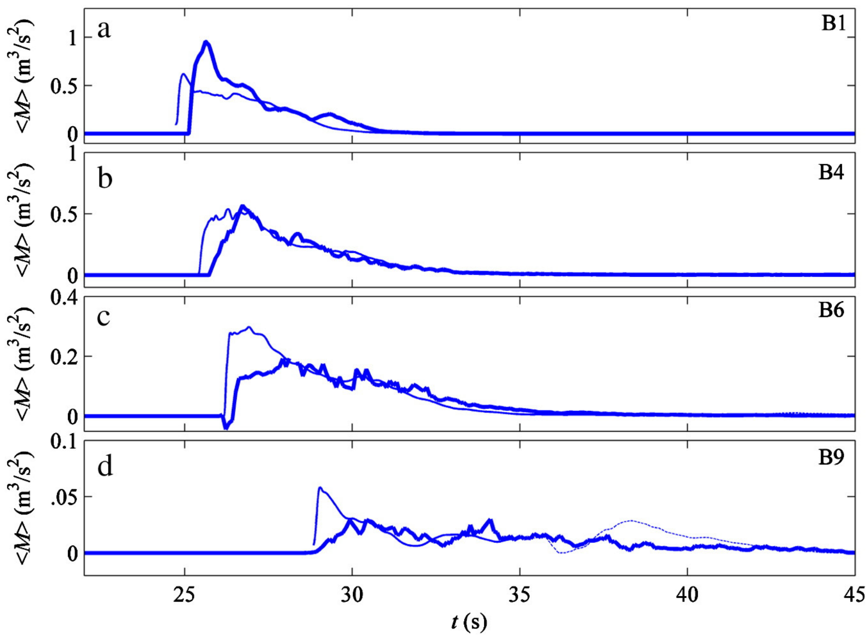

Fig. 9. Comparison of <M> between physical model (thick solid line) and numerical model (solid) at B1, B4, B6 and B9. Where wave reflection is present in the numerical model, the solid line switches to a dashed line.

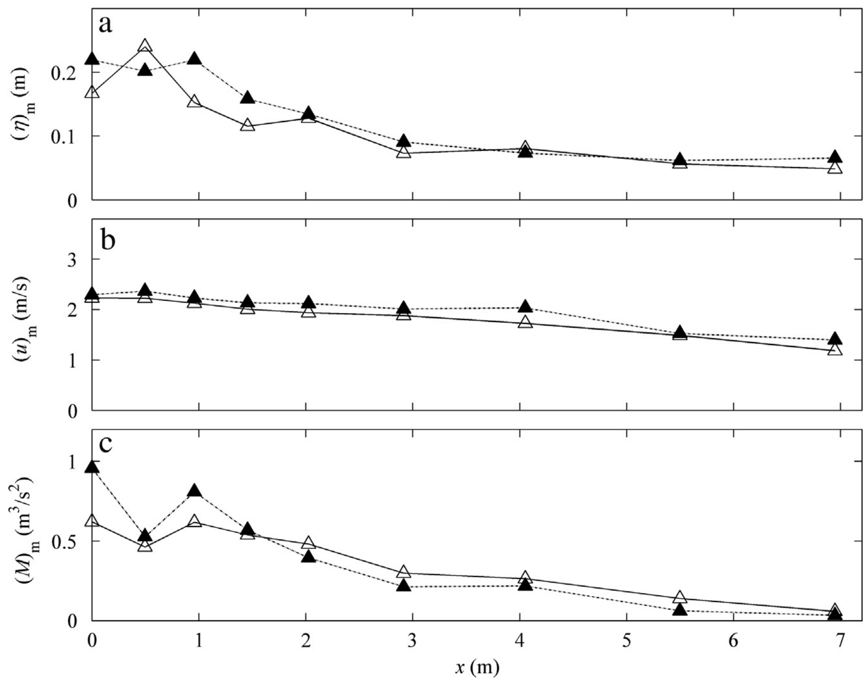

Fig. 10. Comparison of the maximum values between physical model (filled triangle) and numerical model (unfilled triangle) for line B. (a): Maximum free surface elevation, $(\eta)_m$. (b): Maximum cross-shore velocity, $(u)_m$. (c): Maximum specific momentum flux, $(M)_m$.

Overall, with the exception of line D, and line A for velocity, the normalized root mean square errors are less than 0.2.

The normalized root mean square errors for line D are relatively large, and in excess of four times that measured in the other three lines. This anomaly may be attributed to the difference of measurement location. Lines A, B, and C were located on the road, with no obstructions between the locations and the ocean, while line D was located mostly behind buildings. The discrepancy between lines A, B and C and line D may arise from the inherent difficulty of generating an energy dissipation process which includes turbulence in the numerical model, as the broken wave passes around the buildings.

4.1. Model sensitivity for friction factors

To test the numerical model sensitivity, three different friction factors, $f = 0.001$, 0.005 and 0.01, were modeled, and the maximum

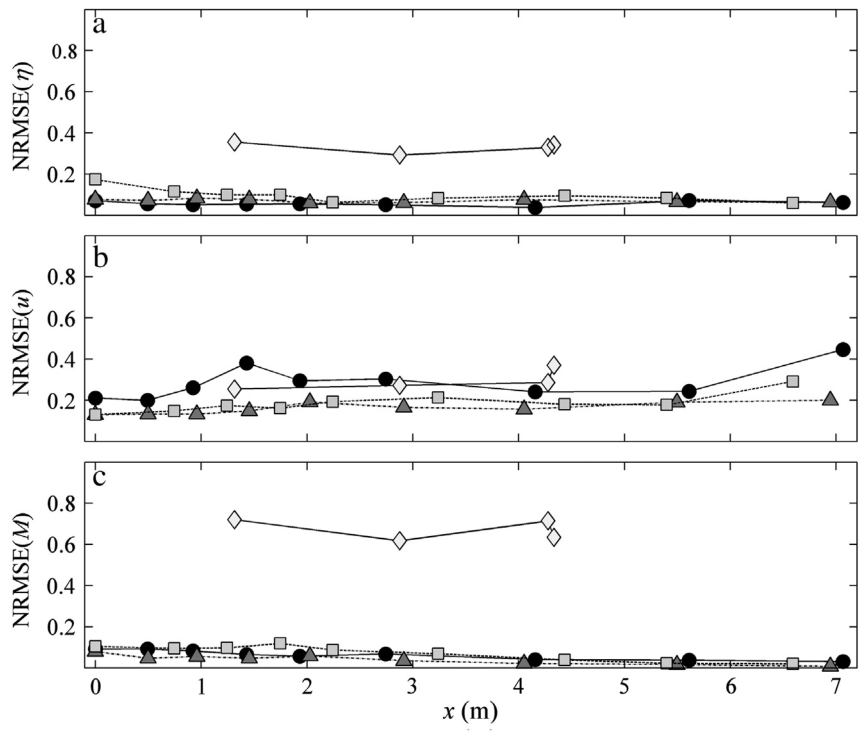

Fig. 11. Normalized root mean square errors (NRMSE) of numerical results at lines A, B, C, and D (circle, triangle, square, and diamond). (a): Free surface elevation, η. (b): Cross-shore velocity, u (c): Specific momentum flux, M.

values of free surface elevation, $(\eta)_m$, velocity, $(u)_m$, and momentum flux, $(M)_m$, were compared to the physical model data as a time series. Fig. 12 shows the comparison between the physical model and numerical model for these friction factors using the maximum values at B1 to B9. The x-axis represents the distance to each measurement location (B1 to B9) in the x-direction from B1. Fig. 12a shows the change in $(\eta)_m$, Fig. 12b shows the change in $(u)_m$, and Fig. 12c shows the change in $(M)_m$. Smaller friction factor values represent less bottom friction; therefore, increased wave magnitude and phase speed are expected as the friction factor decreases. In the numerical model, as f was decreased, the tendencies of $(\eta)_m$, $(u)_m$, and $(M)_m$ remained constant and overall the values increased. The values of $(\eta)_m$ remained relatively unchanged until $x = 4$ m (B1 to B7), after which the fiction factor exhibited a greater influence. As the friction factor decreased by a factor of 10 (from 0.01 to 0.001), the maximum free surface elevation increased an average of 15%, but the cross-shore velocity and specific momentum flux increased 95 and 208%. This fact reveals that the numerical model's velocity and momentum flux terms are highly sensitive to the bottom friction factor. This sensitivity is consistent with modeling of tide and storm surge predictions (e.g., Westerink et al., 1992) and illustrates a potential limitation to using tsunami inundation models verified with bench mark tests with only the maximum free surface elevation. Overall, a friction factor of $f = 0.005$ (triangle) was found to provide results which best matched the physical model.

Fig. 13a, b, and c shows the numerical model sensitivity of η, u, and M, respectively, to the three different friction factors at location B1. When the friction factor was 0.001 (circle), the smallest value, the arrival time of wave was faster than the other two conditions. As the friction factor was increased, the initial magnitude of η, u, and M decreased before $t = 25.3$ s, but after which all only show small changes. It appears that only the leading velocity part was dominated by the friction factors. These results could not be corroborated by the physical model data as only one friction factor was tested.

Fig. 14 shows the same sensitivity test as Fig. 13, but for location B4. Similar to Fig. 13, the arrival time of the inundation wave was earlier and the leading velocity larger as the friction factor decreased. Unlike at location B1, the cross-shore velocity at B4 after $t = 25.3$ s for $f = 0.01$ was noticeably smaller than for the other two friction factors. However, there were still no discernible changes to the free surface elevation due to the various friction factors. The maximum specific momentum flux increased by more than a factor of two as the friction factor decreased from 0.01 to 0.001. This fact highlights the importance of comparing velocity terms in the validation and verification process of numerical models of tsunami inundation when evaluating velocity or force on the structures.

5. Conclusion

This paper presents a comparison of free surface elevation, velocity, and specific momentum flux for tsunami inundation over and around the macro-roughness of a constructed environment between a physical and numerical model (COULWAVE). The physical model was a 1:50 scale idealization of Seaside, Oregon designed to observe the effects of building array and density on tsunami inundation (Fig. 2). In total the free surface elevation and velocity of the inundation flow was measured at 31 locations (Fig. 3). The design wave height was approximately 20 cm, which corresponds to the prototype scale wave height of 10 m (Fig. 4). Measured velocities at the leading edge of the wave were not recorded by the ADV, so leading velocities were determined from optical measurements (Rueben et

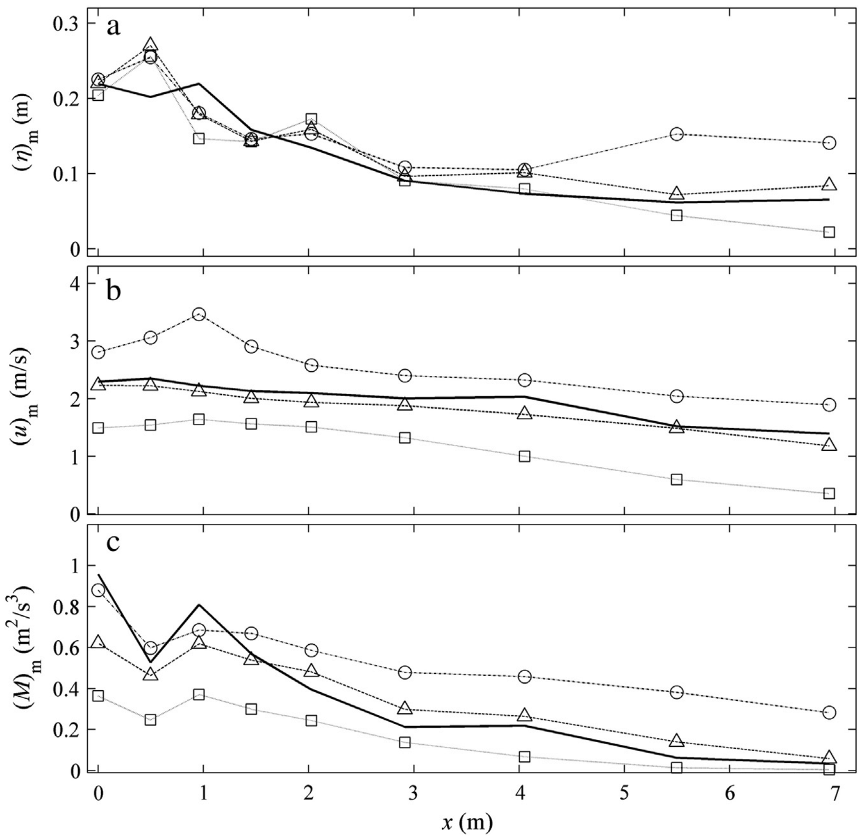

Fig. 12. Numerical model sensitivity test of three friction factors, f = 0.001, 0.005, and 0.01 (circle, triangle, and square), compared to the physical model (solid line) showing maximum values for line B. (a): *(η)m*. (b): *(u)m*. (c): *(M)m*.

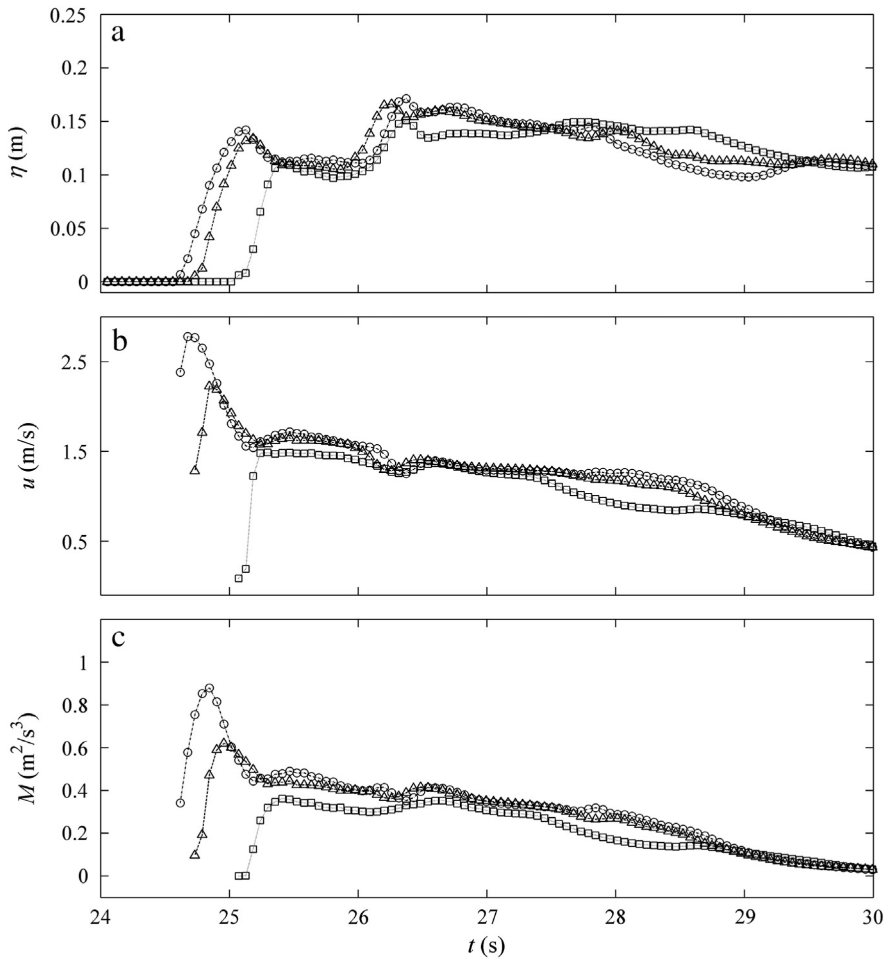

Fig. 13. Numerical model time series sensitivity test of three friction factors, $f = 0.001$, 0.005, and 0.01 (circle, triangle, and square) for location B1.. (a): $(\eta)_m$. (b): $(u)_m$. (c): $(M)_m$.

al., 2010) and interpolated velocity fitting curves applied to calculate the specific momentum flux (Figs. 5 and 6). Primary conclusions are:

1. As the inundating wave propagated around the macro-roughness, the wave shape and location of maximum values of free surface, velocity, and momentum flux changed. If the ensemble average specific momentum flux is calculated using the maximum values of $<\eta>$ and $<u>$, it will be overestimated by approximately 60% at A1 and 260% at A8 (Figs. 5 and 6).
2. In general, the time series and maximum values of free surface elevation, velocity, and specific momentum flux from the numerical model show good agreement with the physical model results (Figs. 7, 8, 9, and 10) except behind the macro-roughness units (Fig. 11, line D).
3. Different friction factors ($f = 0.01$, 0.005 and 0.001) were applied to test the model sensitivity. Result showed that the velocity and flux terms in the numerical model are highly sensitive to the bottom friction factor, while the free surface elevations are only slightly effected. When the friction factor decreased by a factor of 10 (from 0.01 to 0.001), the average maximum free surface elevation only increased 15%, but the average maximum cross-shore velocity and specific momentum flux increased 95 and 208%, respectively (Fig. 12).

This research highlights the importance of comparing velocity terms in the validation and verification process of numerical models of tsunami inundation when evaluating velocity or force on structure. Future research in this area should focus on measuring pressure and force on structures to validate and improve numerical results; model the tsunami return flow, as it is known to induce scour and cause soil instability; and model complex bathymetry and topography.

Nomenclature

Symbol	Description	Units
f	Friction factor	–
H	Total water depth	L
h	Vertical datum	L
M	Momentum flux per unit mass per unit width	L^3T^{-2}
N_T	Number of experiment trials for each measuring location	L
N_V	Available number of measurement data for each measuring location	L
N_η	Recorded number of free surface elevation at each time step	L
N_u	Recorded number of cross-shore velocity at each time step	L
NRMSE	Normalized root mean square error value	–
S	Wave maker displacement	L
s	Second	T
u	Cross-shore (x-axis) velocity	LT^{-1}
u_L	Leading wave velocity	LT^{-1}
v	Along-shore (y-axis) velocity	LT^{-1}
w	Vertical (z-axis) velocity	LT^{-1}
x	x-coordinate in the experiment	L
y	y-coordinate in the experiment	L
η	Free surface elevation	L
η_w	Free surface elevation at wavemaker	L
σ_i	Standard deviation at the specific time, i	L
X_i	Specific measured values (surface elevation) at the time, i	L
$< >$	Ensemble averaged value	–
$(\ )_m$	Maximum value of ( )	–

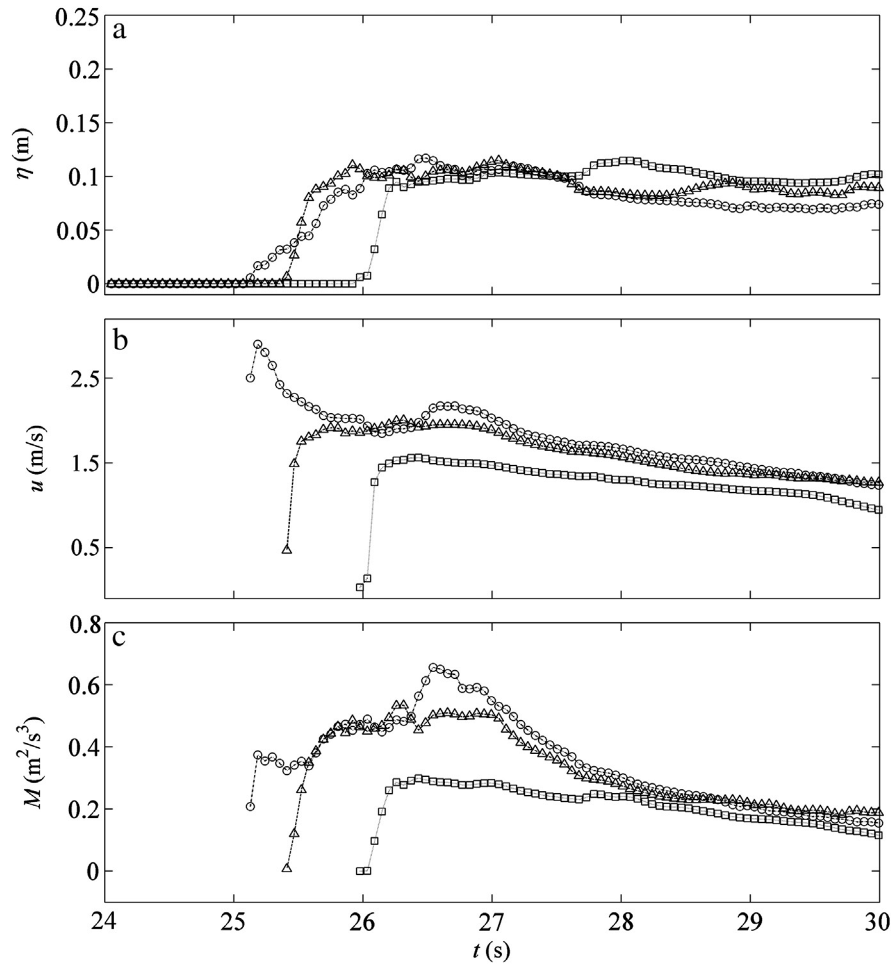

Fig. 14. Numerical model time series sensitivity test of three friction factors, $f = 0.001$, 0.005, and 0.01 (circle, triangle, and square) for location B4. (a): $(\eta)_m$. (b): $(u)_m$. (c): $(M)_m$.

Acknowledgment

This material is based upon work partially supported by the National Science Foundation under Grant No. 0830378 and Oregon Sea Grant under Award No. NB223X. Any opinion, findings, and conclusions or recommendations expressed in this material are those of the authors and do not necessarily reflect the views of the National Science Foundation or Oregon Sea Grant. The authors thank two anonymous reviewers for their constructive comments.

References

Apotsos, A., Jaffe, B., Gelfenbaum, G., 2011. Wave characteristic and morphologic effects on the onshore hydrodynamic response of tsunamis. Coastal Engineering 58, 1034–1048.

Briggs, M., Synolakis, C., Harkins, G., Green, D., 1995. Laboratory experiments of tsunami runup on circular island. Pure and Applied Geophysics 144 (3/4), 569–593.

Cox, D., Tomita, T., Lynett, P., Holman, R., 2008. Tsunami inundation with macro-roughness in the constructed environment. Proc. 31st International Conference on Coastal Engineering, pp. 1421–1432.

Dalrymple, R.A., Kribel, D.L., 2005. The Bridge — Linking Engineering and Society: lessons in engineering from the tsunami in Thailand. National Academy of Engineering 35 (2), 4–14.

DOGAMI (Oregon Department of Geology and Mineral Industries), 2001. “Senate Bill 379.” Portland, OR. Retrieved from: Oregon Geospatial Enterprise Office (GEO) http://cms.oregon.gov/DAS/CIO/GEO/Pages/index.aspx.

FEMA (Federal Emergency Management Agency), 2008. Guidelines for design of structures for vertical evacuation from tsunamis — FEMA P646 Report. Prepared by the Applied Technology Council for the Federal Emergency Management Agency, Redwood City, C.A.

Goldfinger, C., Nelson, C.H., Morey, A.E., Johnson, J.E., Patton, J.R., Karabanov, E., et al., 2012. Turbidite event history—methods and implications for holocene paleoseismicity of the Cascadia subduction zone. U.S. Geological Survey Professional Paper 1661-F. (170 pp.).

Goseberg, N., Schlurmann, T., 2010. Numerical and experimental study on tsunami run-up and inundation influenced by macro roughness elements. Proceedings of the International Conference on Coastal Engineering, p. 32.

Hokkaido Tsunami Survey Group, 1993. Tsunami devastates Japanese coastal region. EOS Transactions of the American Geophysical Union 74 (37), 417–432.

Hughes, S., 1993. Physical models and laboratory techniques in coastal engineering. Advanced Series on Ocean Engineering — Volume 7, World Scientific.

Imamura, F., Koshimura, S., Goto, K., Yanagisawa, H., Iwabuchi, Y., 2006. Global disaster due to the 2004 Indian Ocean tsunami. Journal of Disaster Research 1 (1), 131–135.

Kânoğlu, U., Synolakis, C.E., 1998. Long wave runup on piecewise linear topographies. Journal of Fluid Mechanics 374, 1–28.

Kennedy, A.B., Chen, Q., Kirby, J.T., Dalrymple, R.A., 2000. Boussinesq modeling of wave transformation, breaking and runup. I: 1D. Journal of Waterway, Port, Coastal, and Ocean Engineering 1261, 39–47.

Kim, D.-H., Lynett, P., 2011. Turbulent mixing and scalar transport in shallow and wavy flows. Physics of Fluids 23 (1). http://dx.doi.org/10.1063/1.3531716.

Kim, D.-H., Lynett, P., Socolofsky, S., 2009. A depth-integrated model for weakly dispersive, turbulent, and rotational fluid flows. Ocean Modelling 27 (3–4), 198–214.

Koshimura, S., Oie, T., Yanagisawa, H., Imamura, F., 2009a. Developing fragility functions for tsunami damage estimation using numerical model and post-tsunami data from Banda Aceh, Indonesia. Coastal Engineering Journal 51 (3), 243–273.

Koshimura, S., Namegaya, Y., Yanagisawa, H., 2009b. Tsunami fragility: a new measure to identify tsunami damage. Journal of Disaster Research 4 (6), 479–488.

Liu, P., Yeh, H., Synolakis, C., 2008. Advanced Numerical Models for Simulation Tsunami and Runup. World Scientific Publishing, Singapore.

Lynett, P., 2006. Nearshore modeling using high-order Boussinesq equations. Journal of Waterway, Port, Coastal, and Ocean Engineering (ASCE) 132 (5), 348–357.

Lynett, P., 2007. Effect of a shallow water obstruction on long wave runup and overland flow velocity. Journal of Waterway, Port, Coastal, and Ocean Engineering 133 (6), 455–462.

Lynett, P., Wu, T., Liu, P., 2002. Modeling wave runup with depth-integrated equations. Coastal Engineering 46, 89–107.

Lynett, P., Melby, J., Kim, D.-H., 2010. An application of Boussinesq modeling to hurricane wave overtopping and inundation. Ocean Engineering 37, 135–153.

Mori, N., Takahashi, T., Yasuda, T., Yanagisawa, H., 2011. Survey of 2011 Tohoku earthquake tsunami inundation and run-up. Geophysical Research Letters 38.
Nandasena, N.A.K., Sasaki, Y., Tanaka, N., 2012. Modeling field observations of the 2011 Great East Japan tsunami: efficacy of artificial and natural structures on tsunami mitigation. Coastal Engineering 67, 1–13.
National Oceanic and Atmospheric Administration (NOAA), 2012. National Data Buoy Center. Stennis Space Center, Mississippi. (Retrieved from: National Data Buoy Center. http://www.ndbc.noaa.gov/).
Rueben, M., Holman, R., Cox, D., Shin, S., Killian, J., Stanley, J., 2010. Optical measurements of tsunami inundation through an urban waterfront modeled in a large-scale laboratory basin. Coastal Engineering 58 (3), 229–238.
Shi, Fengyan, Kirby, T., James, Harris, C., Jeffrey, Geiman, D., Joseph, Grilli, T., Stephan, 2012. A high-order adaptive time-stepping TVD solver for Boussinesq modeling of breaking waves and coastal inundation. Ocean Modelling 43–44, 36–51.
Synolakis, C.E., 1987. The runup of solitary waves. Journal of Fluid Mechanics 185, 523–545.
Synolakis, C.a.R.F., 2003. Waves and run-up generated by a three-dimensional sliding mass. Advances in Natural and Technological Hazards Research 19 (1), 113–119.
Synolakis, C., Bernard, E., Titov, V., Kânoğlu, U., Gonzalez, F., 2007. Standards, criteria, and procedures for NOAA evaluation of tsunami numerical models. Commerce, NOAA Tech. OAR PMEL-135.
Titov, V.V., Synolakis, C.E., 1995. Modeling of breaking and non-breaking long wave evolution and runup using VTCS-2. Journal of Waterway, Port, Coastal, and Ocean Engineering 121, 308–316.
Tomita, T., Honda, K., 2007. Tsunami estimation including effect of coastal structures and buildings by 3D model. Coastal Structures 2007, 681–692.
Tomita, T., Honda, K., Kakinuma, T., 2006. Application of storm surge and tsunami simulator in ocean and coastal areas (STOC) to tsunami analysis. Technical Memorandum of Public Works Research Institute 4022.
Tsunami Pilot Study Working Group, 2006. Seaside, Oregon tsunami pilot study—modernization of FEMA flood hazard maps. NOAA OAR Special Report, NOAA/OAR/PMEL, Tsunami Pilot Study Working Group.
Westerink, J.J., Luettich, R.A., Baptista, A.M., Scheffner, N.W., Farrar, P., 1992. Tide and storm surge predictions using finite element model. Journal of Hydraulic Engineering 118 (10), 1373–1390.
Yeh, H., 2006. Maximum fluid forces in the tsunami runup zone. Journal of Waterway, Port, Coastal, and Ocean Engineering 132 (6), 496–500.
Yeh, H., Liu, P., Synolakis, C., 1996. Long-wave Runup Models. World Scientific, Singapore.
Yeh, H., Sato, S., Tajima, Y., 2012. The 11 March 2011 East Japan earthquake and tsunami: tsunami effects on coastal infrastructure and buildings. Pure and Applied Geophysics. http://dx.doi.org/10.1007/s00024-012-0489-1 (in press).